Int. J. Heat Mass Transfer. Vol. 35, No. 6, pp. 1481–1494, 1992
Printed in Great Britain

0017–9310/92 $5.00 + 0.00

Mixed convection in a horizontal rectangular channel—experimental and numerical velocity distributions

THOMAS A. NYCE, JALIL OUAZZANI, ARNAUD DURAND-DAUBIN† and FRANZ ROSENBERGER

Center for Microgravity and Materials Research, University of Alabama in Huntsville, Huntsville, AL 35899, U.S.A.

(*Received* 21 *March* 1991 *and in final form* 14 *May* 1991)

Abstract—Mixed convection in a rectangular channel (width/height = 2) with bottom-heated and top-cooled sections is studied by laser Doppler anemometry in nitrogen at $Ra = 22\,200$ and $Re = 18.75$, 36 and 54. At the lower Re values symmetry breaking is observed in steady but spatially oscillating flows that prevail over a certain distance from the leading edge of the differentially heated section. Further downstream unsteady flows are found even for $Re = 18.75$. Numerical models are used to investigate the effects of: adiabatic, conducting (with a conductive–convective heat transfer coefficient) and perfectly conducting side walls; channel tilts and Prandtl number dependence. Good agreement between calculations and experiment is obtained for longitudinal convective roll velocities. The transverse velocities are found to be independent of Re.

1. INTRODUCTION

MIXED CONVECTION, i.e. the interplay of forced and buoyancy-driven convection, in rectangular ducts or channels plays an important role in various technological processes, such as the chemical vapor deposition (CVD) of solid layers [1, 2], or the cooling of electronic equipment [3, 4]. In particular in CVD, the superposition of transverse, buoyancy-driven flow and longitudinal, forced flow can lead to rather nonuniform layer thickness and composition distributions. Since these nonuniformities are often detrimental for device applications, many of the experimental and numerical investigations of mixed convection in channels [5–18] are motivated by the desire to supply a fluid dynamic underpinning for better CVD reactor designs. Earlier numerical work on mixed convection [5–9] was based on the assumption that axial momentum diffusion can be neglected, i.e. that the flow is parabolic and, thus, can be well described by the results of a computer-time saving marching technique. However, experimental [16] and fully three-dimensional numerical flow studies [16–18] have shown that even at relatively high Reynolds numbers significant flow reversal effects can occur in the vicinity of the leading edge of the bottom heated plate, which cannot be recovered with a marching technique.

Earlier laser Doppler anemometry (LDA) work in our group [13, 14] was concerned with the characterization of the entrance effects and fully developed flow of mixed convection between the differentially heated horizontal plates of a channel with a cross-sectional aspect ratio (width/height) of 10. In order to minimize the thermophoretic deflection [19] of seed particles required in LDA studies, the large temperature gradients characteristic of CVD processes must be avoided. Fortunately, by taking advantage of the strong temperature dependence of the thermophysical properties of gases, one can obtain the high Rayleigh numbers, Ra, typical for CVD operations, in simulations that are conducted near room temperature with rather small temperature gradients. In these investigations, we found that at combinations of low Reynolds numbers, Re, and high Ra values, the admixture of transverse and longitudinal convection rolls resulted in unsteady flow in the form of a 'snaking' motion. Furthermore, we showed analytically and experimentally that the transverse velocity of the longitudinal rolls is independent of the Re of the forced flow.

In order to obtain insight into the mixed convection behavior in a geometry that more closely resembles that of actual CVD reactors we have, in the present investigation, expanded our earlier work to a horizontal channel with a cross-sectional aspect ratio of 2. Applying the same experimental techniques as in refs. [13, 14], we have mapped the velocity distributions in the bottom-heated channel with low velocity laser Doppler anemometry for $Ra = 22\,200$ and a range of Reynolds numbers ($Re = 18.75$, 36 and 54). We have also modeled these experiments numerically, employing parabolic and full 3-D finite volume codes. The effects of three lateral thermal boundary conditions were investigated: adiabatic and perfectly conducting side walls, and conducting walls of finite width with a conductive–convective heat transfer condition on the outer surface. In addition, effects of channel

† On leave from Institut de Mécanique des Fluides de Marseille, Université d'Aix-Marseille II, Marseille 13003, France.

NOMENCLATURE

AR	aspect ratio = width/height	u, v, w	velocity components in the x-, y- and z-directions
g	gravitational acceleration	u_0	average inlet velocity
h	heat transfer coefficient between side wall and ambient, see equation (13)	$\mathbf{v}$	velocity vector, (u, v, w)
		W	width of the channel
H	height of the channel	x, y, z	Cartesian coordinates.
k	thermal conductivity of gas		
k_w	thermal conductivity of wall	Greek symbols	
Pr	Prandtl number, ν/κ	β	thermal expansion coefficient
Ra	Rayleigh number, $\beta g \Delta T H^3/\nu\kappa$	θ	dimensionless temperature
Re	Reynolds number, $u_0 H/\nu$	κ	thermal diffusivity
T	temperature of gas	ν	kinematic viscosity
T_c	temperature of top plate and isothermal entrance section	ρ	density of gas.
T_h	temperature of bottom plate in heated section	Other symbols	
		∇	nabla operator
ΔT	$T_h - T_c$	∇^2	Laplacian operator.

tilts about the longitudinal axis and of a small variation of the Prandtl number were explored numerically.

2. EXPERIMENTAL APPARATUS AND TECHNIQUE

The experimental arrangement and conditions in this study were identical to those employed in refs. [13, 14], except for the inner height and width of the channel, which were 2.5 and 5 cm, respectively. As in our earlier studies, an isothermal section of the channel, long enough to ensure a hydrodynamically fully developed flow, was smoothly joined to a differentially heated section of the same aspect ratio (Fig. 1). The bottom wall of this downstream section was isothermally heated to T_h, whereas the top wall was kept at the temperature of the isothermal entrance section, T_c. While the top and bottom walls of the channel consisted of thermostatted metal plates, with a measured temperature uniformity of ± 0.2°C, the side walls were made of 1.27-cm-thick Plexiglas™, the outer surface of which was exposed to the ambient. For the highest Reynolds number of 54, the momentum entrance length for a rectangular channel of these dimensions is 12 cm, and the thermal entrance length is 8.5 cm [11, 20–22]. We used a 40-cm-long entrance section to allow for the decay of perturbations in the velocity field that result from the expanding flow from the tubular gas supply line. The full development of a Poiseuille velocity profile upstream of the differentially heated section was anemometrically verified. The heated section was 81 cm long, i.e. much longer than the thermal entrance length given in the literature for the hydrodynamic development of flows with $Re = 54$ in differentially heated channels with high aspect ratios [10]. In all runs we used nitrogen, a vertical temperature difference $\Delta T = T_h - T_c = 15$°C and an average temperature of 27.5°C, at which the transport coefficients of the gas were evaluated. This resulted in a Rayleigh number, based on the channel height, of 22 200. Since the channel's side walls consisted of Plexiglas™, the experimental thermal boundary conditions, relative to heat transport in the gas, were between adiabatic and conducting. This is important for the comparison between experimental and numerical results.

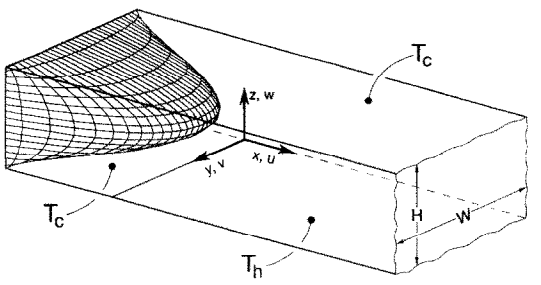

FIG. 1. Definition sketch for 3-D channel used for mixed convection studies, with isothermal entrance section followed by bottom heated section.

3. NUMERICAL MODEL

3.1. *Geometry*

As depicted in Fig. 1, the height of the rectangular channel is denoted by H and its width by W. The aspect ratio $AR = W/H$ is 2. A Cartesian coordinate system is used with the x-axis and y-axis, respectively, parallel and perpendicular to the forced flow direction. The z-axis is antiparallel to the gravity vector. The velocity field of the monocomponent gas entering the differentially heated section of the channel at $x = 0$

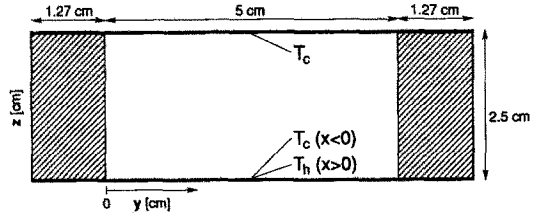

FIG. 2. Cross-section (y–z plane) of channel including Plexiglas® side walls.

is assumed to be fully developed. In some of the numerical runs we have accounted for heat conduction through the side walls of finite thickness (see Fig. 2).

3.2. *Transport equations*

The governing equations were cast in dimensionless form using H, u_0 (where u_0 is the average velocity at the inlet), ρu_0^2 and $T_h - T_c$ to scale the lengths, velocity, pressure and temperature, respectively. In the Boussinesq approximation, steady-state transport in this horizontal configuration is then governed by the following system of coupled dimensionless conservation equations for mass, momentum and energy:

$$\nabla \cdot \mathbf{v} = 0 \tag{1}$$

$$\nabla \cdot (\mathbf{vv}) = -\nabla p + \frac{1}{Re}\Delta \mathbf{v} + \frac{Ra}{Re^2\, Pr}\theta \mathbf{e} \tag{2}$$

$$\nabla \cdot (\mathbf{v}\theta) = \frac{1}{Pr\, Re}\nabla \theta \tag{3}$$

where $\mathbf{v}$, $\theta = (T - T_c)/(T_h - T_c)$ and p, respectively, represent the dimensionless velocity, temperature and pressure, and $\mathbf{e}$ is the unit vector in the z-direction. The dimensionless parameters $Pr = \nu/\kappa$, $Ra = \beta g \times (T_h - T_c)H^3/\nu\kappa$ and $Re = u_0 H/\nu$ are, respectively, the Prandtl, Rayleigh and Reynolds numbers [13, 14].

3.3. *Boundary conditions*

The boundary conditions for the above set of equations are as follows. On the walls the normal and tangential velocities are zero

$$u = v = w = 0. \tag{4}$$

At the inlet ($x = 0$) the fluid has an axial velocity according to a Poiseuille profile [18, 23, 24] and

$$v = w = 0. \tag{5}$$

At the outlet of the channel, we impose a pressure boundary condition for velocities and a given fixed temperature, which are calculated a priori for each case by considering the flow as parabolic. In such parabolic calculations the exit conditions are part of the solution. We will further discuss this point in the final section.

The temperature at the inlet, top of the channel and bottom of the isothermal section is

$$T = T_c \tag{6}$$

whereas at the bottom of the heated section

$$T = T_h. \tag{7}$$

As a first approach, the side walls were assumed to be adiabatic, i.e.

$$\frac{\partial T}{\partial y} = 0. \tag{8}$$

We have also simulated perfectly conducting side walls by imposing on the inner surface a fixed profile which was obtained as a solution of a 2-D heat conduction problem in a wall between two parallel plates, the upper plate being at T_c, and the lower plate being at T_c for $x < 0$ and T_h for $x > 0$. However, in the actual experiment, the side wall temperatures also depend on the heat losses to the ambient, and can be approximated by solutions to the heat transfer problem discussed next.

3.4. *Heat transfer to and from side walls*

The side wall temperatures are modeled as the result of heat transfer by convection and conduction. Due to the low temperature and temperature differences involved in the experiments, heat transfer by radiation is neglected. The heat conduction in the channel wall is described by the equation

$$\nabla^2 T = 0. \tag{9}$$

For the boundary conditions we assume at the inner wall

$$k_w\left(\frac{\partial T_w}{\partial n}\right) = k\left(\frac{\partial T}{\partial n}\right) \tag{10}$$

where k_w (4.962×10^{-4} g-cal cm^{-1} s^{-1} K^{-1} [25]) and k (0.839×10^{-4} g-cal cm^{-1} s^{-1} K^{-1} [26]) are the thermal conductivities of the wall and the fluid, respectively, the partial derivatives are with respect to the normal to the wall and T_w is the temperature on the inner surface of the side walls. At the wall's outer surface, the boundary condition represents the balance of energy conducted through the wall with energy lost to the surroundings. It has the form

$$-k_w\left(\frac{\partial T_w}{\partial n}\right) = h(T_w - T_\infty) \tag{11}$$

where T_∞ is the temperature of the ambient and h is an overall heat transfer coefficient

$$h = 1.42\left(\frac{T_h - T_c}{H}\right)^{1/4} \quad [\mathrm{W\,m^{-2}\,^\circ C^{-1}}] \tag{12}$$

which we have estimated from correlations for conductive–convective heat transfer on vertical walls [27]. Similar treatments of the heat losses from side walls of CVD reactors, including radiative heat transfer, were used in refs. [17, 28].

3.5. *Method of solution*

The set of equations (1)–(3) and boundary conditions (4)–(12) were solved using the finite volume

code PHOENICS [18, 29]. We have previously used this code for the MOCVD of GaAs [18, 30]. Due to the iterative process of the code, boundary conditions such as (10) and (11) can be satisfied at convergence, which we considered as reached when the maximum algebraic residual in all equations was smaller than 10^{-6}.

The mesh used had, respectively, 81, 30 and 15 grid points in the x-, y- and z-directions for all cases with adiabatic or conducting side walls. When heat transfer through the side walls was incorporated in the computations, 42 grid points were used in the y-direction, with six grid points in each side wall. The computations were performed on a Cray XMP supercomputer. The CPU times for a typical full 3-D case (51 200 cells) were 2–3 h and for 3-D parabolic cases 5–15 min.

4. RESULTS

In the following we combine the presentation of experimental and numerical results and group them according to the main flow characteristics observed.

4.1. *Symmetric, steady flow with spatial oscillations* ($Re = 36$)

For this medium Reynolds number case the average inlet flow velocity was 2.3 cm s^{-1}. The numerical solutions presented in Figs. 3–7 were obtained for side walls with the heat transfer conditions introduced in Section 3.4. The surfaces in Fig. 3 represent the axial component (u) of the velocity in the y–z plane at $x = 5$ and 20 cm, with experimental and numerical results in good agreement at both locations. Figures 4–6 show the transverse components (v, w) of the velocity and the resulting temperature fields in the cross-sectional planes at $x = 2$, 5 and 20 cm. One sees that buoyancy-driven rolls parallel to the side walls develop quickly, significantly modulating the in-flowing Poiseuille profile in the axial velocity from the beginning of the bottom-heated section.

For a more quantitative comparison we have illustrated the evolution of the experimental and numerical $u(y)$ profiles in the channel's mid-height plane ($z = 1.25$ cm) with a sequence of presentations for various x-locations in Figs. 7(a) and (b). These figures show an excellent agreement between experimental data and computed results over the entire length of the channel.

A detailed analysis of the extensive experimental data obtained at this medium Reynolds number shows that the flow is symmetric about the plane $y = 2.5$ cm and steady throughout the channel. Interestingly, the experimental data show a distinct spatial oscillation in the magnitude of the axial velocity $u(y)$ in which momentum is periodically transferred between the two maxima and the minimum. Figure 8 shows that the period of the oscillation is about 5 cm, and the amplitude is ± 0.4 cm s^{-1}. The numerical data do not show any oscillation but represent the spatial average well.

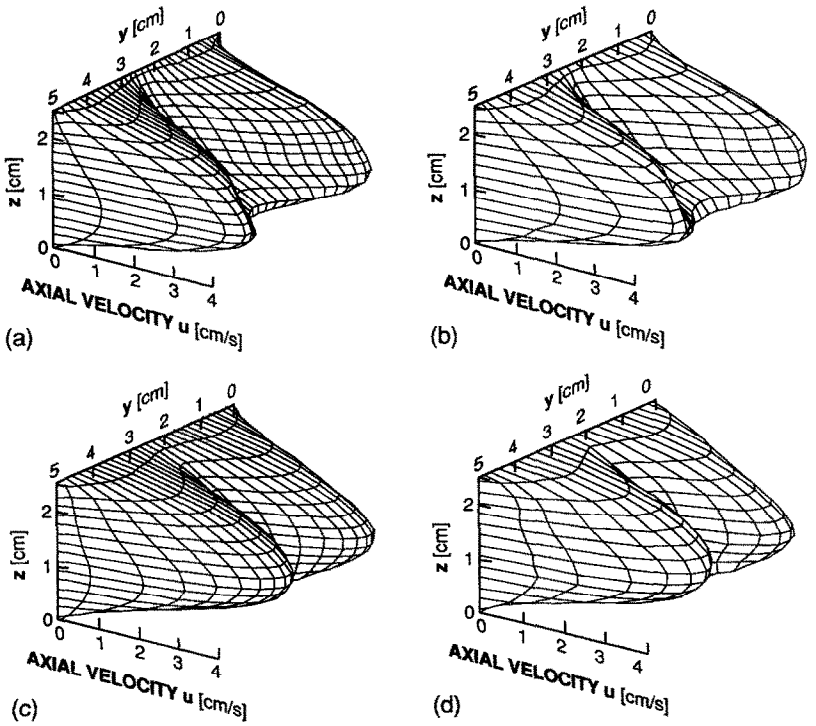

FIG. 3. Comparison of experimental and numerical velocity distributions. Surfaces for axial velocity component (u) in y–z planes for $Re = 36$: numerical (a) and experimental (b) at $x = 5$ cm; numerical (c) and experimental (d) at $x = 20$ cm.

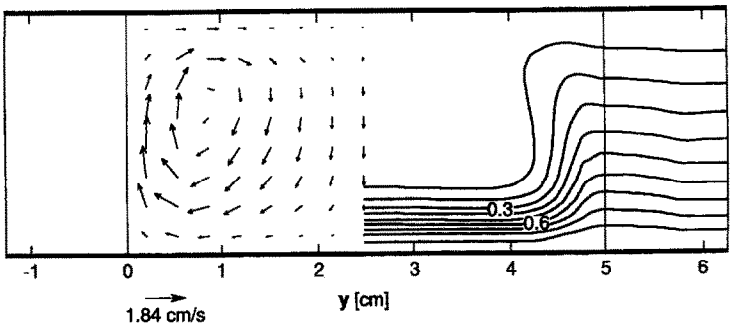

FIG. 4. Calculated distributions of transverse velocity (left side) and dimensionless temperature (right side) at $x = 2$ cm for $Re = 36$.

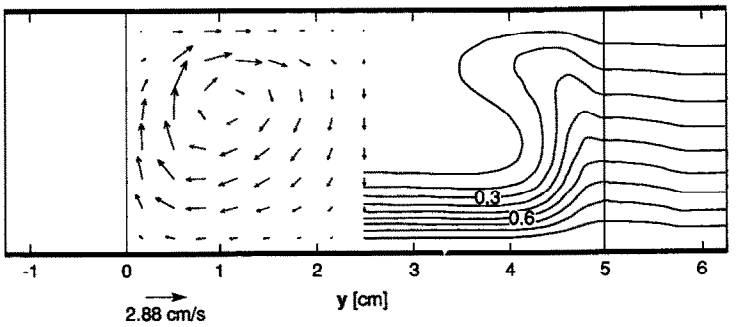

FIG. 5. Calculated distributions of transverse velocity (left side) and dimensionless temperature (right side) at $x = 5$ cm for $Re = 36$.

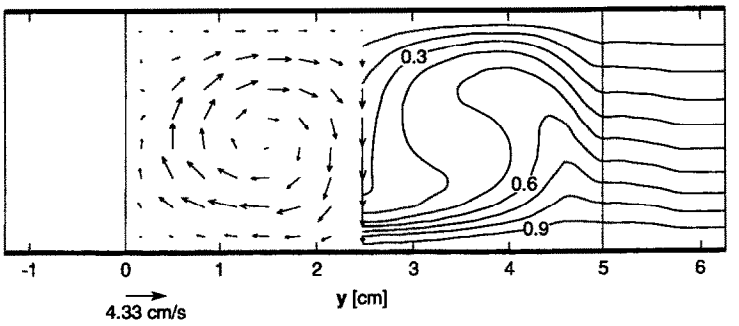

FIG. 6. Calculated distributions of transverse velocity (left side) and dimensionless temperature (right side) at $x = 20$ cm for $Re = 36$.

4.2. *Asymmetric, unsteady flow* ($Re = 18.75$)

For this lowest Reynolds number case the average inlet flow velocity was 1.18 cm s^{-1}. Figures 9(a) and (b) illustrate the evolution of the axial velocity profile $u(y)$ with increasing axial distance x from the leading edge of the heated plate, measured in the half-height plane ($z = 1.25$ cm). Note that even at $x = 0$, the profile is already significantly deformed as compared to the upstream Poiseuille profile. At this low Re (i.e. relatively low forced velocity), the buoyancy-driven transverse recirculation roll that tends to form in the axial temperature gradient at about $x = 0$ actually leads to a slight flow reversal ($u < 0$) in the experimental data even at mid-height between 3.5 cm $< x < 6$ cm. Note that the numerical results exhibit this reversal already at $x = 2.5$ cm.

The main finding in this lowest Re case, however, is an interesting asymmetry about the mid-width plane ($y = 2.5$ cm). As shown in Figs. 9(a) and (b), the maxima in the axial velocity, that arise from the two longitudinal rolls in the $AR = 2$ channel, alternate in magnitude with increasing x. This asymmetry has been emphasized in the figures by horizontal dashed lines through the respective left maximum of the experimental $u(y)$ data. Equally important, this spatial unsteadiness gives way to a temporally unsteady

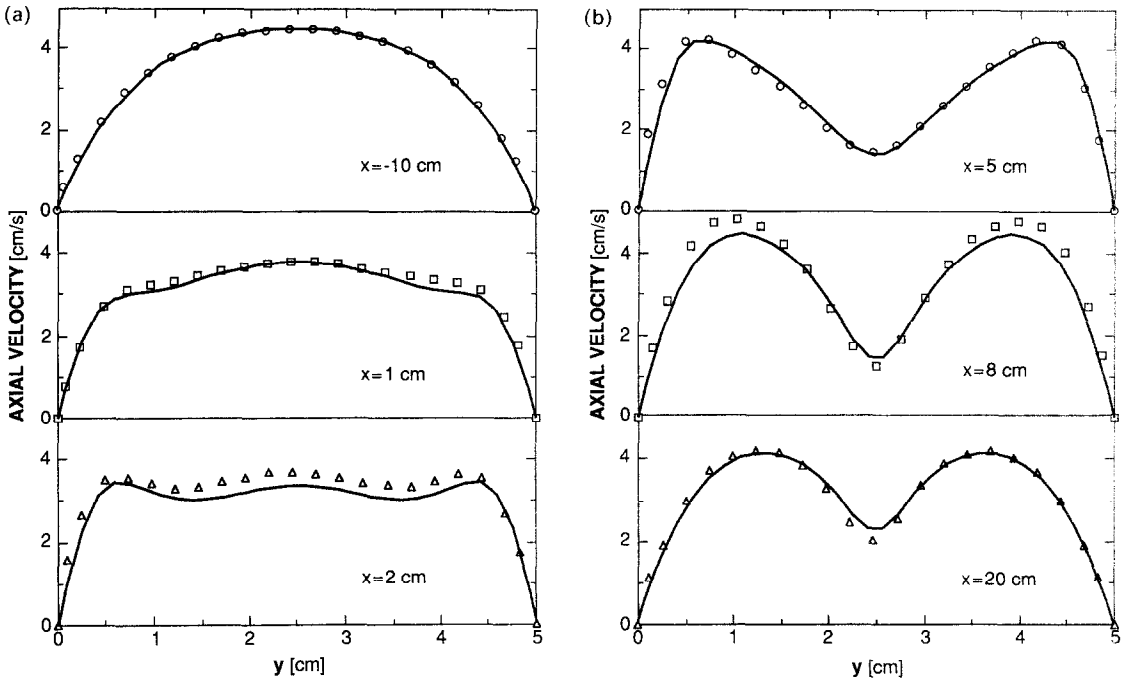

FIG. 7. Comparison of experimental (symbols) and numerical axial velocities (curves) $u(y)$ at mid-height ($z = 1.25$ cm) at various axial locations for $Re = 36$.

flow behavior for $x > 12$ cm. Note that the numerical simulation does not give this asymmetry and a steady-state solution is found for the whole length of the channel. However, simulations for a channel with a tilt about the x-axis as small as 2° yielded asymmetries of equal or greater magnitude than those shown by the experiments. This is illustrated in Fig. 10(a), which presents computed $u(y)$ profiles obtained for the tilted model together with experimental data for the 'untilted' channel. In contrast to Fig. 9, the asymmetries in the numerical profiles are now emphasized by the dashed horizontal lines. Figure 10(b) illustrates the evolution of the numerical axial velocity with increasing x for two symmetric locations ($y = 1$ and 4 cm) at mid-height ($z = 1.25$ cm). A comparison of these curves with the data of Fig. 9 shows that the period in the magnitude of the maxima in $u(y)$ is much longer in the numerical simulations. We have not been able to obtain steady-state solutions for a tilt angle of 7 . Unfortunately, we could not perform unsteady 3-D

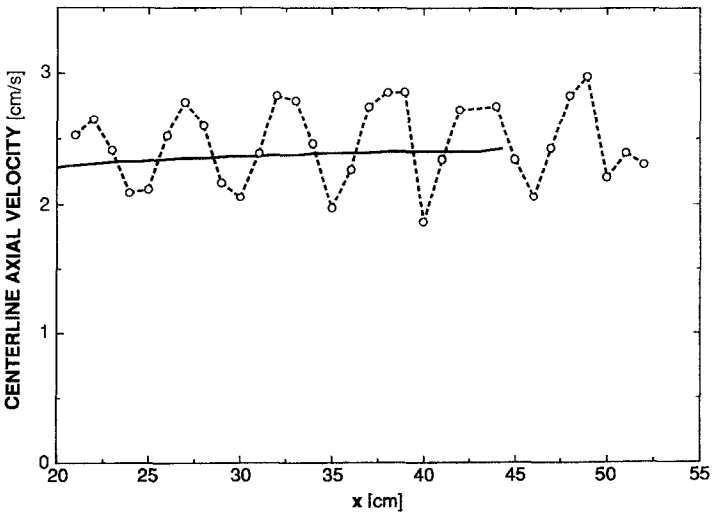

FIG. 8. Comparison of experimental and numerical axial velocities as a function of axial distance x, measured along centerline ($z = 1.25$ cm, $y = 2.5$ cm) for $Re = 36$.

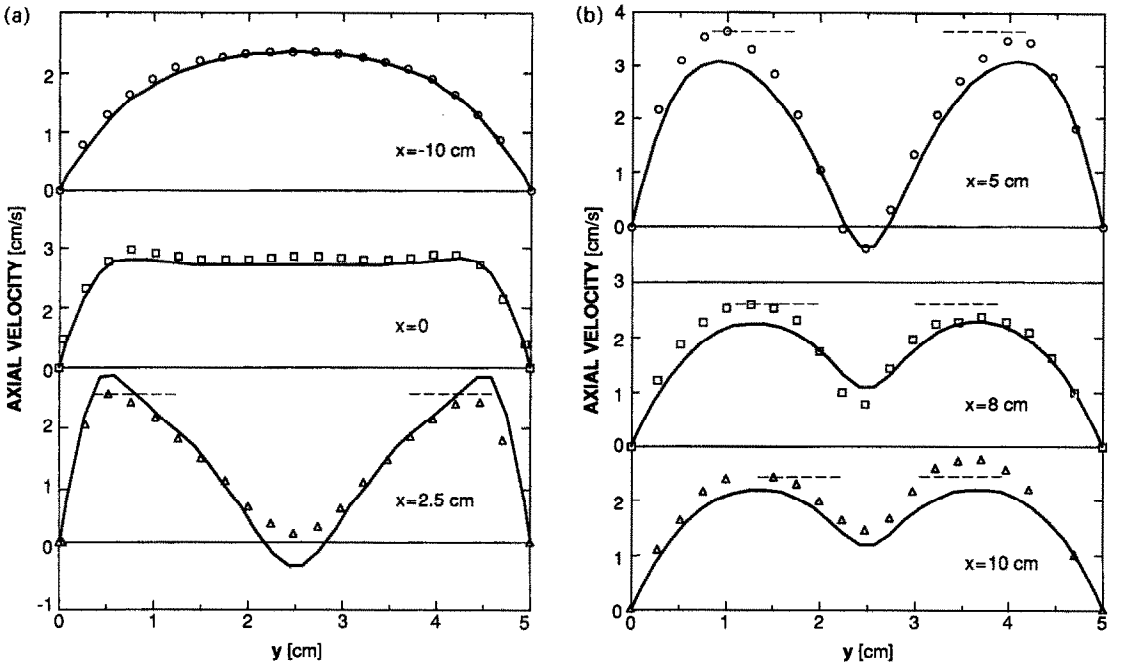

FIG. 9. Comparison of experimental and numerical axial velocities $u(y)$ at mid-height ($z = 1.25$ cm) at various axial locations for $Re = 18.75$.

calculations for this large domain due to the exorbitant CPU time and memory size required for such a computation. Hence, we assume that the asymmetries present in the experimental data are due to a small, practically difficult to characterize, misalignment of the channel from the horizontal. This insight is particularly important, since in the CVD practice such small misalignments will always be present, and thus lateral asymmetries in the growth rates will be difficult to avoid at low flow rates. It should be noted that

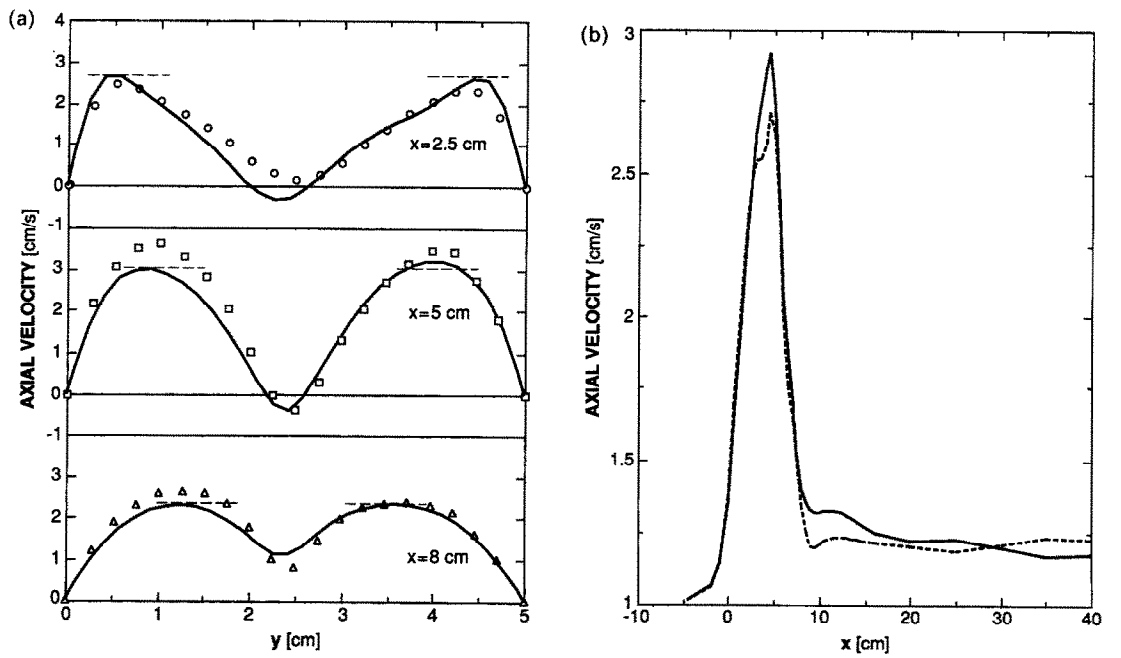

FIG. 10. Mixed convection at $Re = 18.75$ and a tilt angle of 2°. (a) Comparison of experimental and numerical axial velocities $u(y)$ at mid-height ($z = 1.25$ cm) at various axial locations. (b) Evolution of the numerical axial velocity u along the x-direction for two symmetric locations at mid-height ($z = 1.25$ cm): $y = 1$ cm (dashed line) and $y = 4$ cm (solid line).

similar symmetry breaking has been observed before in numerical CVD work by Fotiadis and Jensen [31].

Figures 11–13 show the transverse components (v, w) of the velocity and the resulting temperature fields in the cross-sectional planes at $x = 1$, 2.5 and 8 cm for this low Reynolds number case. A comparison with the solutions for $Re = 36$ in Figs. 4–6 indicates again a more rapid development of the rolls in the entrance region.

4.3. *Symmetric, steady flow* ($Re = 54$)

Figure 14 presents experimentally and numerically obtained axial velocity surfaces at $x = 8$ and 40 cm for this case with the highest average inlet flow velocity of 3.5 cm s^{-1}. Again experimental and numerical data compare well in both the entrance and fully developed regions. Figures 15–17 show that, as compared to the lower Re cases, the flow field as well as the temperature distribution take longer to become fully developed. Figure 18 illustrates that the numerical and experimental data are essentially in quantitative agreement. Furthermore, we see that in this case the flow is symmetric about the mid-width plane and shows no spatial oscillations in the x-direction. While this is a significant difference from the lower Re cases, one cannot exclude the possibility that such oscillations may still develop in channels longer than that used in our experiments.

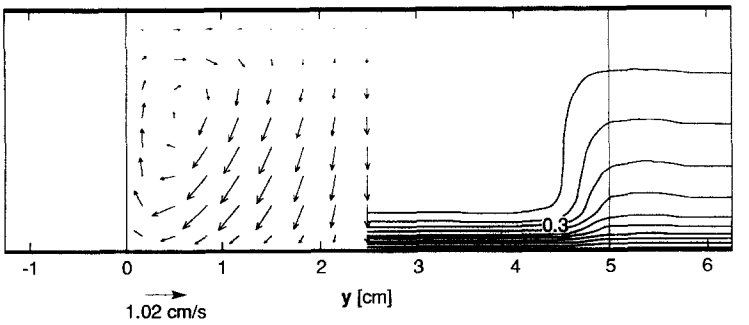

FIG. 11. Calculated distributions of transverse velocity (left side) and dimensionless temperature (right side) at $x = 1$ cm for $Re = 18.75$.

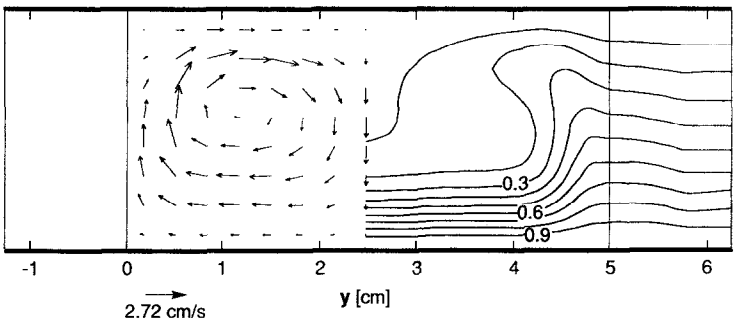

FIG. 12. Calculated distributions of transverse velocity (left side) and dimensionless temperature (right side) at $x = 2.5$ cm for $Re = 18.75$.

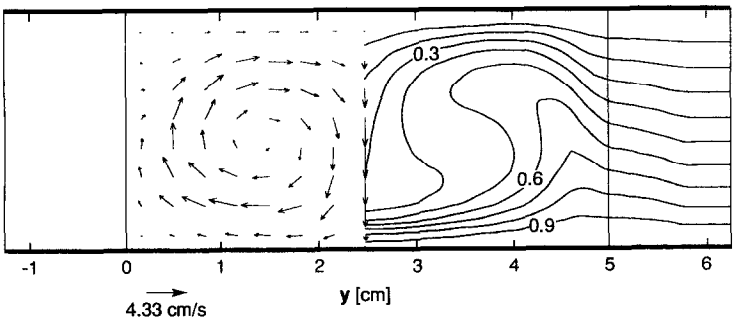

FIG. 13. Calculated distributions of transverse velocity (left side) and dimensionless temperature (right side) at $x = 8$ cm for $Re = 18.75$.

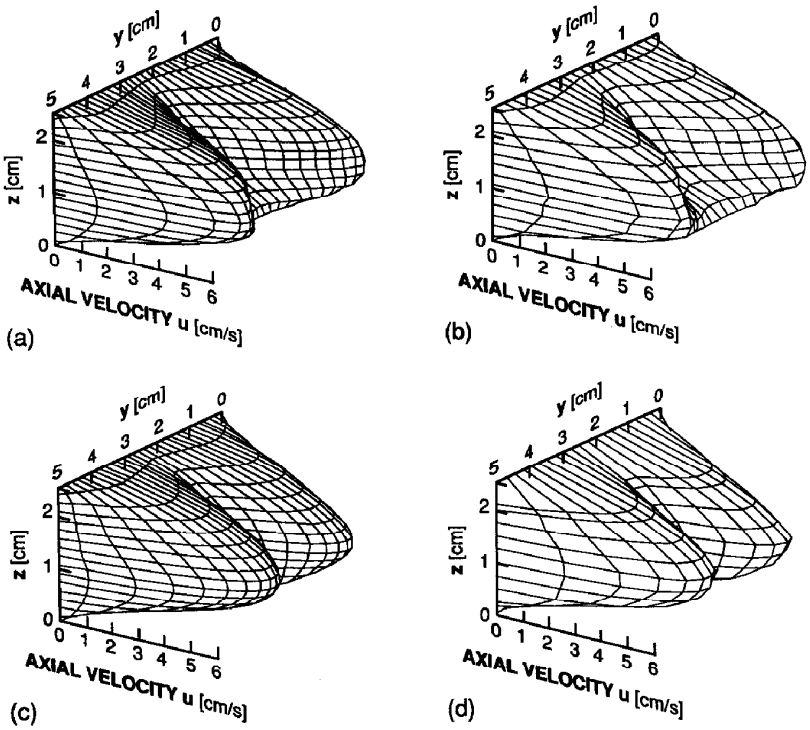

FIG. 14. Comparison of experimental and numerical velocity distributions. Surfaces for axial (u) velocity component in y–z planes for $Re = 54$ at $x = 8$ cm: numerical (a) and experimental (b); and at $x = 40$ cm: numerical (c) and experimental (d).

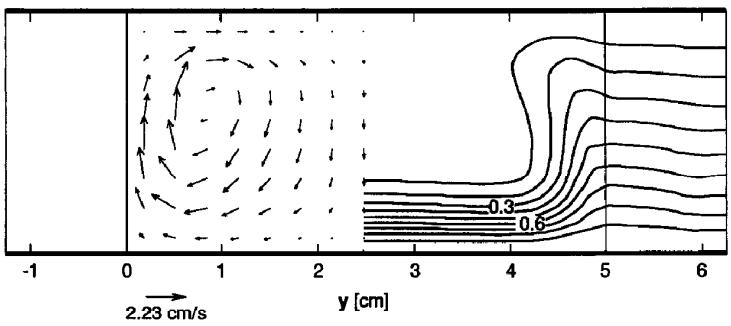

FIG. 15. Calculated distributions of transverse velocity (left side) and dimensionless temperature (right side) at $x = 2$ cm for $Re = 54$.

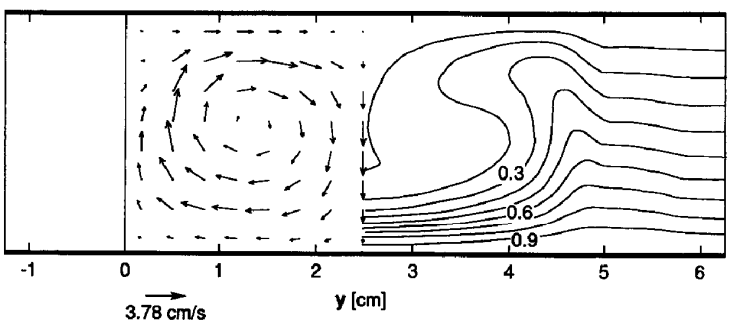

FIG. 16. Calculated distributions of transverse velocity (left side) and dimensionless temperature (right side) at $x = 8$ cm for $Re = 54$.

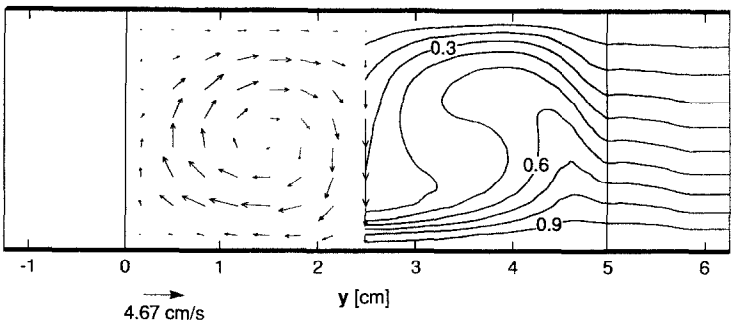

FIG. 17. Calculated distributions of transverse velocity (left side) and dimensionless temperature (right side) at $x = 40$ cm for $Re = 54$.

4.4. *Effect of wall boundary conditions*

In the experimental apparatus the thermal conductivity of the side walls was approximately six times that of the gas. Hence, one should expect the numerical solutions for conducting side walls to be much closer to the experimental data than those for adiabatic side walls. Figure 19 confirms this expectation. Note that the solutions for the perfectly conducting and the conductive–convective thermal boundary conditions are practically indistinguishable and, hence, presented as one curve. Also noteworthy is that the differences between experiment and adiabatic computation are largest in the entrance region, where the velocity profile develops slower than with conducting side walls. At larger downstream distances, however, where the mixed convection flow is more developed, the proper lateral boundary condition becomes less important, as one can see from the good fit between experimental data and numerical results for adiabatic side walls at $x = 20$ cm. This is further illustrated by the side wall temperature contours displayed in Fig. 20. The largest differences occur in the entrance region, where heat conduction in the walls leads to a much more rapid increase of T_{wall} with z than in the adiabatic case; yet, even farther downstream there are significant differences in the wall temperature distribution resulting from the two boundary conditions. The warmer walls of the conducting case, in turn, destabilize the flow more readily and the rolls form at much shorter distances than in the adiabatic case. This nicely illustrates the importance of the proper thermal boundary conditions in the numerical modeling of actual experiments, as pointed out in refs. [7, 9, 30].

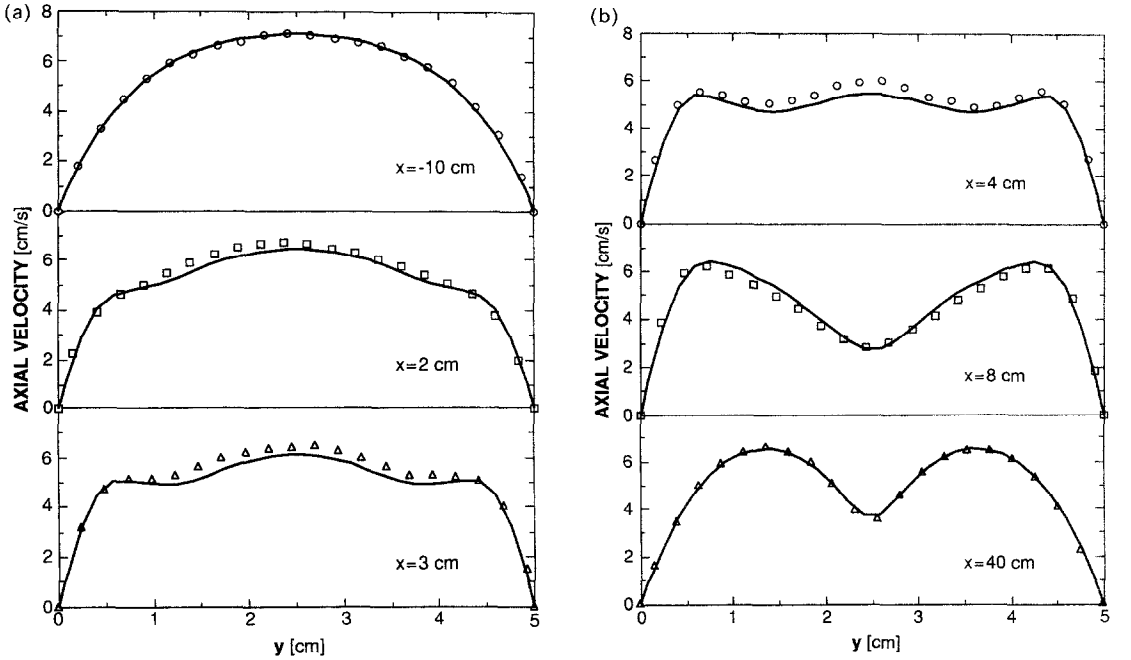

FIG. 18. Comparison of experimental and numerical axial velocities $u(y)$ at mid-height ($z = 1.25$ cm) at various axial locations for $Re = 54$.

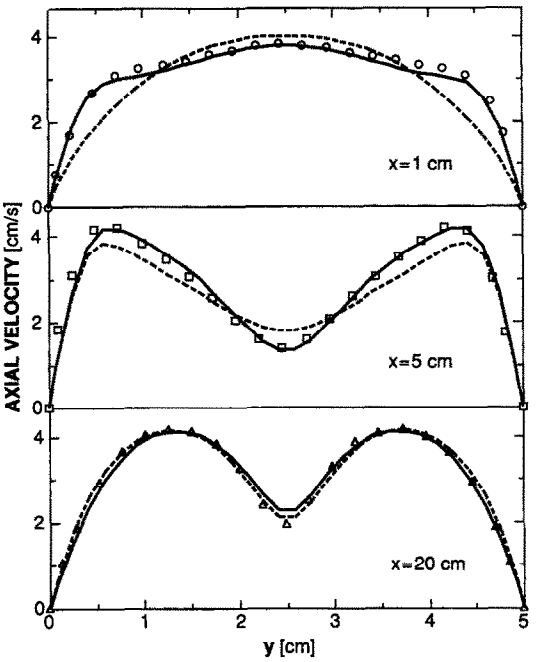

FIG. 19. Comparison of experimental and numerical axial velocities $u(y)$ at mid-height ($z = 1.25$ cm) at various axial locations for $Re = 36$. Dashed and solid lines are, respectively, for adiabatic and conducting side walls in the numerical model.

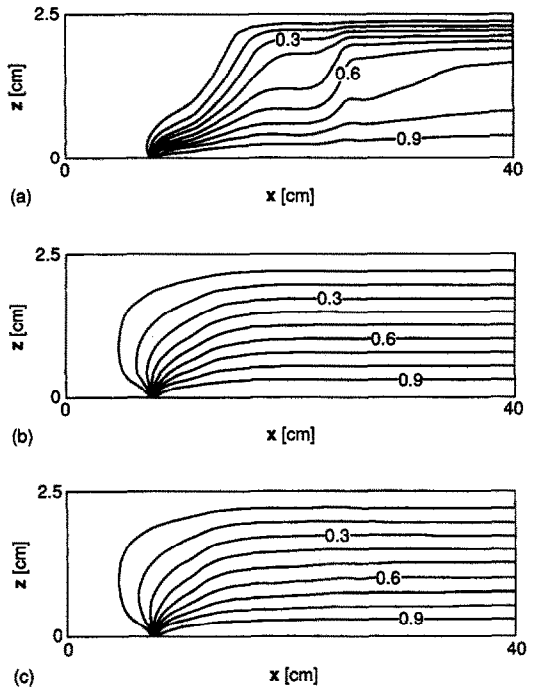

FIG. 20. Calculated dimensionless temperature distributions on inner surface of channel side wall for $Re = 36$ obtained with adiabatic (a), imposed conducting (b) and conductive–convective (c) heat transfer conditions.

4.5. *Independence of transverse velocity on Reynolds number*

Earlier we have shown analytically as well as experimentally with a channel of aspect ratio 10 [14] that the transverse velocities of longitudinal rolls forming at sufficiently high Ra in mixed convection are independent of the strength, i.e. Re, of the forced flow contribution. Figure 21 shows the numerical transverse velocity profiles for the three different Reynolds numbers considered in this work at $x = 40$ cm. The comparison of these three profiles confirms that the transverse velocities for the fully developed flow are independent of Re even for small aspect ratio channels.

4.6. *Sensitivity to Prandtl number and elliptic vs parabolic simulation*

In order to explore the effect of (small) variations in the Prandtl number we have, in addition to the above solutions for $Pr = 0.71$, obtained numerical results for $Pr = 1$ for the $Re = 36$ case. Figure 22 shows that, as a result of this seemingly insignificant increase in Pr, the development of the flow in the channel is slowed, leading to a significant increase in entrance length. Similar to the comparison of the flow development under adiabatic and conductive boundary conditions above, the fully developed solutions for these two Prandtl numbers are identical. Quantitatively, we see that a change of 20% in the Prandtl number can lead to more than 40% change in the entrance length, i.e. the distance required for the flow to become fully developed. This underlines the importance of the Prandtl number, which is sometimes not properly accounted for in discussions of buoyancy-driven flows.

In a previous paper on channel flows [18] we have shown that, though 3-D parabolic calculations led to significant savings in computer time as compared to a full 3-D model, the application of this economical option is limited to large aspect ratio channels and high Re values. To further illustrate this, we have compared in the present work the results of the 3-D parabolic and full 3-D elliptic codes for the highest Reynolds number, $Re = 54$. Figure 23 shows that the parabolic option slows the development of the velocity profile, in poor agreement with the experimental findings. Thus, even at this relatively high Re, the parabolic option is not very accurate for the flow development at this high Ra in the low aspect ratio channel. At large downstream distances, however, the two codes give practically identical solutions. Hence, we have advantageously used the parabolic solutions at the exit of the channel to define the exit boundary conditions for the elliptic computations.

5. SUMMARY

Our experimental study of mixed convection in a horizontal channel at $Ra = 22\,000$ has revealed three flow regimes as a function of Reynolds number. At

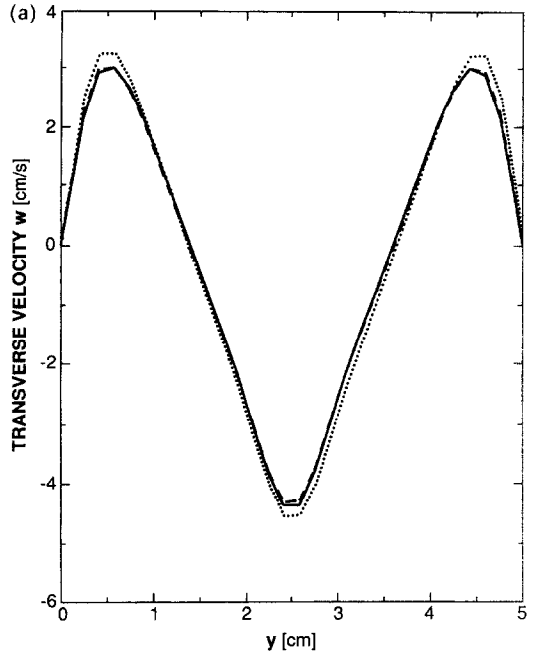

FIG. 21. Comparison of numerical transverse velocities $w(y)$ at mid-height ($z = 1.25$ cm) at $x = 40$ cm for $Re = 18.75$ (solid curve), $Re = 36$ (dashed curve) and $Re = 54$ (dotted curve).

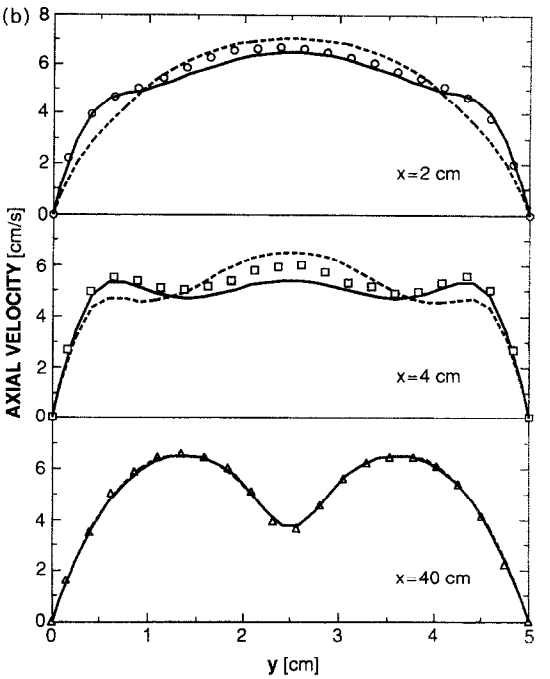

FIG. 23. Comparison of experimental and numerical axial velocities $u(y)$ at mid-height ($z = 1.25$ cm) at various axial locations for $Re = 54$ obtained with full 3-D code (solid curves) and parabolic 3-D code (dashed curves).

$Re = 18.75$, buoyancy-driven rolls develop very quickly, significantly modulating the axial velocity even in cross-sections close to, but clearly upstream of, the heated section. In the heated section ($x > 0$), with increasing downstream distance, the flow is first steady but asymmetric, and eventually becomes unsteady. These asymmetries have been predicted theoretically [32], but experimental evidence has not been published prior to this work. A small tilt angle, as low as 2°, can produce sufficient numerical perturbations to introduce spatial oscillations in the solutions at low enough Reynolds numbers. At $Re = 36$, the axial velocity at $x = 0$ is only slightly modified. Although the flow remains steady and symmetric about the vertical plane through the mid-width, there is a small spatial oscillation in the velocities over the length of the channel. The period of this oscillation was around 5 cm. At $Re = 54$, the longitudinal rolls developed smoothly over a length of 30 cm, with no asymmetries, unsteadiness or spatial oscillations.

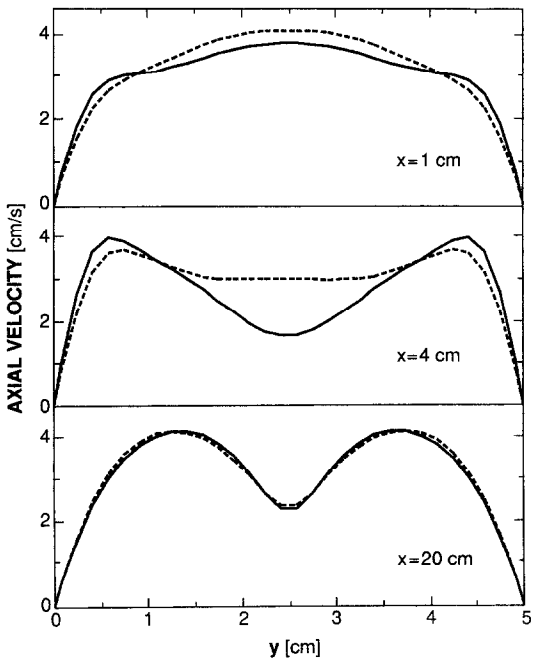

FIG. 22. Comparison of numerical axial velocities $u(y)$ at mid-height ($z = 1.25$ cm) at various axial locations for $Re = 36$ and $Pr = 0.71$ (solid curves) and $Pr = 1$ (dashed curves).

Numerical simulations of these experiments reveal the importance of the use of proper thermal boundary conditions on the side walls. While good agreement was obtained between experimental velocity distributions and those obtained for conductive boundary conditions, adiabatic side walls resulted in good agreement only at large x. In the developing region, adiabatic conditions suppress the development of the buoyancy-driven flow features. As in our earlier work on mixed convection in a horizontal channel of $AR = 10$, the transverse velocities of the longitudinal rolls in the channel with $AR = 2$ and the flow conditions studied here were found to be independent of Re. Furthermore, we have shown that in the developing flow region the effects of small variations in the Prandtl number can be significant even at relatively

high Reynolds numbers. Finally, it is important to note that even at the highest *Re* dealt with here, the mixed flow cannot be considered as parabolic but requires an elliptical treatment for high fidelity modeling.

Acknowledgements—The authors thank Lynne Carver for the graphics support; Dwight Goodman, Dave Adams and Peter Mutaftschiev for their contributions to the experimental work; and Melissa Rogers for careful proof reading of the manuscript. Research support by the Microgravity Science and Applications Division of the National Aeronautics and Space Administration under Grant NAG8-704, and by the State of Alabama through the Center for Microgravity and Materials Research at the University of Alabama in Huntsville and the Alabama Supercomputer Network, is also gratefully acknowledged.

REFERENCES

1. D. W. Hess, K. F. Jensen and T. J. Anderson, Chemical vapor deposition: a chemical perspective, *Rev. Chem. Engng* **3,** 97–186 (1985).
2. K. F. Jensen, Micro-reaction engineering applications of chemical engineering to processing of electronic and photonic materials, *Chem. Engng Sci.* **42,** 923–958 (1987).
3. M. E. Braaten and S. V. Patankar, Analysis of laminar mixed convection in shrouded arrays of heated rectangular blocks, *Int. J. Heat Mass Transfer* **28,** 1699–1709 (1985).
4. K. J. Kennedy and A. Zebib, Combined free and forced convection between horizontal planes: some case studies, *Int. J. Heat Mass Transfer* **26,** 471–474 (1983).
5. R. Takahashi, Y. Koga and K. Sugawara, Gas flow pattern and mass transfer analysis in a horizontal flow reactor for chemical vapor deposition, *J. Electrochem. Soc.* **119,** 1406–1412 (1972).
6. F. P. Incropera and J. A. Schutt, Numerical simulation of laminar mixed convection in the entrance region of horizontal rectangular ducts, *Numer. Heat Transfer* **8,** 707–729 (1985).
7. H. K. Moffat and K. F. Jensen, Complex flow phenomena in MOCVD reactors. I: Horizontal reactors, *J. Crystal Growth* **77,** 108–119 (1986).
8. H. V. Mahoney, F. P. Incropera and S. Ramadhyani, Development of laminar mixed convection flow in a horizontal rectangular duct with uniform bottom heating, *Numer. Heat Transfer* **12,** 137–155 (1987).
9. H. K. Moffat and K. F. Jensen, Three-dimensional flow effects in silicon CVD in horizontal reactors, *J. Electrochem. Soc.* **135,** 459–471 (1988).
10. G. J. Hwang and K. C. Cheng, Convective instability in thermal entrance region of a horizontal parallel-plate channel heated from below, *J. Heat Transfer* **95,** 72–77 (1973).
11. H. Morihara and R. T.-S. Cheng, Numerical solution of the viscous flow in the entrance region of parallel plates, *J. Comput. Phys.* **11,** 550–572 (1973).
12. L. J. Giling, Gas flow patterns in horizontal epitaxial reactor cells observed by interference holography, *J. Electrochem. Soc.* **129,** 634–644 (1982).
13. K.-Ch. Chiu and F. Rosenberger, Mixed convection between horizontal plates—I. Entrance effects, *Int. J. Heat Mass Transfer* **30,** 1645–1654 (1987).
14. K.-Ch. Chiu, J. Ouazzani and F. Rosenberger, Mixed convection between horizontal plates—II. Fully developed flow, *Int. J. Heat Mass Transfer* **30,** 1655–1662 (1987).
15. J. Ouazzani, K.-Ch. Chiu and F. Rosenberger, On the 2-D modelling of CVD reactors and its limitations, *J. Crystal Growth* **91,** 497–508 (1988).
16. E. P. Visser, C. R. Kleijn, C. A. M. Govers, C. J. Hoogendoorn and L. J. Giling, Return flows in horizontal MOCVD reactors studied with the use of TiO_2 particle injection and numerical calculations, *J. Crystal Growth* **94,** 929–946 (1989).
17. C. R. Kleijn and C. J. Hoogendoorn, A study of 2-D and 3-D transport phenomena in horizontal chemical vapor deposition reactors, *Chem. Engng Sci.* **46,** 321–334 (1991).
18. J. Ouazzani and F. Rosenberger, Three-dimensional modelling of horizontal chemical vapor deposition—I. MOCVD at atmospheric pressure, *J. Crystal Growth* **100,** 545–576 (1990).
19. L. Talbot, R. K. Cheng, R. W. Schefer and D. R. Willis, Thermophoresis of particles in a heated boundary layer, *J. Fluid Mech.* **101,** 737–758 (1980).
20. G. S. Beavers, E. M. Sparrow and R. A. Magnuson, Experiments on hydrodynamically developing flow in rectangular ducts of arbitrary aspect ratio, *Int. J. Heat Mass Transfer* **13,** 689–702 (1970).
21. S. T. McComas, Hydrodynamics entrance lengths for ducts of arbitrary cross-section, *J. Basic Engng* **89,** 847–850 (1967).
22. H. Schlichting, *Boundary Layer Theory* (7th Edn), p. 186. McGraw-Hill, New York (1972).
23. R. K. Shah and A. L. London, *Laminar Flow Forced Convection in Ducts*, p. 197. Academic Press, New York (1978).
24. F. W. White, *Viscous Fluid Flow*, p. 123. McGraw-Hill, New York (1974).
25. F. M. Hernan and J. I. Kroschwitz (Editors), *Encyclopedia of Polymer Science and Technology*, Vol. 13, p. 780. Wiley, New York (1985).
26. W. M. Kays and M. E. Crawford, *Convective Heat and Mass Transfer* (2nd Edn), p. 389. McGraw-Hill, New York (1980).
27. W. H. McAdams, *Heat Transmission* (3rd Edn), pp. 233–238. McGraw-Hill, New York (1954).
28. D. I. Fotiadis, M. Boekholt, K. F. Jensen and W. Richter, Flow and heat transfer in CVD reactors: comparison of Raman temperature measurements and finite element model predictions, *J. Crystal Growth* **100,** 577–599 (1990).
29. S. V. Patankar, *Numerical Heat Transfer and Fluid Flow*. Hemisphere, New York (1980).
30. J. Ouazzani and F. Rosenberger, Three-dimensional numerical modelling of transport in horizontal CVD reactors. In *Chemical Vapor Deposition 1990* (Edited by G. W. Cullen and K. Spear), pp. 82–91. Electrochemical Society, Pennington, New Jersey (1990).
31. D. I. Fotiadis and K. F. Jensen, Symmetry breaking phenomena in vertical and horizontal CVD reactors. In *Chemical Vapor Deposition 1990* (Edited by G. W. Cullen and K. Spear), pp. 92–98. Electrochemical Society, Pennington, New Jersey (1990).
32. J. Watson, On spatially-growing finite disturbances in plane Poiseuille flow, *J. Fluid Mech.* **14,** 211–221 (1962).

CONVECTION MIXTE DANS UN CANAL HORIZONTAL RECTANGULAIRE—DISTRIBUTIONS EXPERIMENTALES ET NUMERIQUES DES VITESSES

Résumé—La convection mixte dans un canal rectangulaire (largeur/hauteur = 2), avec une section chaude en haut et froide en bas, est étudié par anémométrie laser Doppler dans l'azote à $Ra = 22\,200$ et $Re = 18{,}75$, 36 et 54. Aux plus faibles valeurs de Re, on observe la cassure de la symétrie dans les écoulements permanents mais spatialement oscillants qui existent à une certaine distance du bord d'attaque de la section. Des écoulements instables subsistent en aval même pour $Re = 18{,}75$. Des modèles numériques permettent d'étudier les effets des parois adiabatiques, conductrices (avec un coefficient de transfert thermique conductif–convectif), parfaitement conductrices, et des inclinaisons du canal ainsi que de la dépendance au nombre de Prandtl. On obtient un bon accord entre calculs et expérience pour les vitesses des rouleaux convectifs longitudinaux. Les vitesses transversales sont trouvées indépendantes de Re.

EXPERIMENTELL UND NUMERISCH BESTIMMTE GESCHWINDIGKEITSVERTEILUNGEN BEI DER MISCHKONVEKTION IN EINEM WAAGERECHTEN RECHTECKKANAL

Zusammenfassung—Die Mischkonvektion in einem Rechteckkanal (Breite/Höhe = 2) mit beheizten Abschnitten in der unteren, und gekühlten Abschnitten in der oberen Fläche wird mit Hilfe der Laser-Doppler-Anemometrie für folgende Bedingungen in Stickstoff untersucht: $Ra = 22\,200$; $Re = 18{,}75$; 36 und 54. Bei den kleinen Re-Zahlen bricht die Symmetrie in stationäre aber räumlich oszillierende Strömungen auf, die von der Anströmkante an über einen bestimmten Bereich des unterschiedlich beheizten Abschnitts vorherrschen. Weiter stromabwärts ergeben sich nichtstationäre Strömungen-sogar bei $Re = 18{,}75$. Mit Hilfe numerischer Modelle werden folgende Einflüsse untersucht: Seitenwände, die entweder adiabat oder leitend (mit einem Wärmeübergangskoeffizienten für Leitung und Konvektion) oder perfekt leitend sind; unterschiedliche Kanalneigungen sowie unterschiedliche Prandtl-Zahlen. Für die Konvektionswalzen in Längsrichtung der Strömung ergibt sich zwischen berechneten und gemessenen Ergebnissen gute Übereinstimmung. Die quergerichteten Geschwindigkeiten erweisen sich als von der Reynolds-Zahl unabhängig.

СМЕШАННАЯ КОНВЕКЦИЯ В ГОРИЗОНТАЛЬНОМ КАНАЛЕ ПРЯМОУГОЛЬНОГО СЕЧЕНИЯ ЭКСПЕРИМЕНТАЛЬНОЕ И ЧИСЛЕННОЕ ОПРЕДЕЛЕНИЕ РАСПРЕДЕЛЕНИЙ СКОРОСТЕЙ

Аннотация—С использованием лазер-допплеровской анемометрии исследуется смешанная конвекция в канале прямоугольного сечения (отношение ширины к высоте равно двум), нижняя часть которого нагревается, а верхняя охлаждается при $Ra = 22\,200$ и $Re = 18{,}75$; 36 и 54. В случае низких значений Re наблюдалось нарушение симметрии стационарных, но пространственно осциллирующих течений, имеющих место на некотором расстоянии от передней кромки участка с переменным нагревом. Далее в направлении течения наблюдались нестационарные режимы даже при $Re = 18{,}75$. Численные модели использовались для исследования эффектов адиабатических с конечной проводимостью (с коэффициентом кондуктивно-конвективного теплопереноса) и идеально проводящих боковых стенок, а также зависимости от наклона канала и числа Прандтля. Получено удовлетворительное согласие между расчетами и экспериментальными данными для продольных скоростей конвективных валов. Найдено, что поперечные скорости не зависят от значения Re.